Finite Element Analysis of Stimulated Brillouin Scattering in Integrated Photonic Waveguides

Björn C. P. Sturmberg ⓘ, Kokou Bertin Dossou ⓘ, Michael J. A. Smith ⓘ, Blair Morrison, Christopher G. Poulton ⓘ, and Michael J. Steel ⓘ

Abstract—**We describe a finite element algorithm for modeling stimulated Brillouin scattering in optical waveguides of arbitrary cross-section. The method allows rapid calculation of optical and elastic dispersion relations, field profiles, and gain. Additionally, we provide an open and extensible set of standard problems and reference materials to facilitate the bench-marking of our solver against subsequent tools. Such a resource is needed to help settle discrepancies between existing formulations and implementations, and to facilitate comparison between results in the literature. The resulting standardized testing framework will allow the community to gain confidence in new algorithms and will provide a common tool for the comparison of experimental designs of opto-acoustic waveguides.**

Index Terms—Computational acoustics, computational electromagnetism, finite element method, opto-acoustics, stimulated Brillouin scattering.

I. INTRODUCTION

THE rapid growth of interest in stimulated Brillouin scattering (SBS) in integrated waveguides [1]–[3] has generated a need for new numerical tools for the analysis of integrated devices and their opto-elastic coupling.[1] The complex geometries required for the mutual confinement of light and sound, the sensitive dependence on waveguide materials and configuration, as well as the possibility of strongly anisotropic elastic properties, calls for advanced and precise tools that meet the requirements of experimental design and interpretation. Currently researchers rely on a mix of commercial and in-house software, including bespoke routines that vary substantially between research groups. The variety of formulations and implementations, together with the intricacy of the problem and the absence of standardized tests, makes it challenging to reproduce existing results and thereby to validate one's own calculations. This task is made more difficult by the fact that in certain waveguide geometries and SBS configurations, some effects contribute very little or cancel out, but dominate when a different geometry or configuration is used. This means that errors either in the underlying equations or in the implementation can be well hidden, and there is currently no universally-accepted simulation package that can be used to validate new results. Moreover, even assuming identical formulations and implementations of the opto-elastic waveguide problem, there is substantial literature variation in the numerical values of material properties, both elastic and optical, again making tests against earlier results difficult. Indeed, for many contemporary materials such as soft glasses, the elastic properties have never been reliably measured at all. The community would benefit greatly from an open library of reference problems that can be continually expanded.

Here we present a finite-element based algorithm specifically designed to carry out SBS calculations for longitudinally invariant waveguides. We demonstrate the tool by computing both forward and backward Brillouin gain spectra for both inter- and intra-mode scattering, as well as generating the optical and elastic modes. Other key quantities needed for the design of SBS-active waveguides and for the interpretation of experiments are also provided, such as elastic quality factors. The implementation accounts for both electrostrictive/photoelastic and radiation pressure/moving boundary effects. We use a fully-tensorial formulation for the computation of the mechanical problem, so that elastically anisotropic materials can be examined. A subclass of optically anisotropic materials is also supported. The algorithm can also be used to compute the elastic wave loss if

[1]The stimulated Brillouin literature frequently refers to both "acoustic" and "elastic" waves interchangeably. Here we favor the word "elastic" which carries a stronger connotation of waves in solids.

the material components of the viscosity tensor are known. The implementation automatically identifies the symmetry class of optical and elastic fields to help identify suitable mode combinations for efficient opto-elastic coupling [4] and to facilitate understanding of the complex families of elastic dispersion relations and crossings that are typically found in these calculations. Our tool is freely available as an extensible open-source package named NumBAT, the *Numerical Brillouin Analysis Tool* [5].

The algorithm presented here uses two fast Fortran-based two-dimensional Finite Element Method (FEM) routines that solve for the optical and elastic modes of arbitrary longitudinally invariant waveguides; the electromagnetic solver is an extension of [6], while the acoustic mode-solver is new and has been designed to easily implement the phase-matching conditions required for the Brillouin interaction. All materials are assumed to be optically linear and non-magnetic, and while their elastic properties may be fully anisotropic, their permittivity tensor must (currently) be at most uniaxially anisotropic. Our calculations are explicitly restricted to ideal longitudinally-invariant structures and as explored in [7], longitudinal variations in waveguides can significantly affect the SBS gain and must be accounted for. However in such cases, the outputs of our solver, both modal profiles and gains, will be important as they are the key inputs to coupled mode treatments of longitudinally varying structures, provided the variation is slow compared to the optical and elastic wavelengths.

The algorithm and code presented here builds on a significant body of work on the simulation of Brillouin processes. In particular, FEM routines have previously been used to compute the strength of Brillouin coupling, either via mode overlap [8]–[10], or by adding a driving term, arising from the optical field, to the elastodynamic equations [11]–[14]. Our approach computes the opto-elastic properties in the stimulated Brillouin scattering framework developed by Wolff *et al.* [10]; this framework takes into account the tensorial nature of the opto-mechanical interaction, as well as avoiding questions involving the interpretation of optical momenta in materials. In preparation for this article we have confirmed the compatibility of the formalism of Wolff *et al.* with others in the literature, including those of Rakich *et al.* [2], Florez *et al.* [15] and Sipe and Steel [16].

Geometries and materials are specified in a class-based Python front-end with classes representing the familiar tensors or elastic moduli and related parameters. The Python interface provides access to all values and geometries required by typical users, and enables the use of the extensive suite of Python libraries, such as `numpy`, `scipy` and `matplotlib`, for convenient data analysis and multiprocessing. In this paper we present the full formalism, discuss various pitfalls that can arise in both the analysis and in the numerics, and provide details of the open-source implementation of the resulting algorithm [5], [17].

The remainder of this paper is organized as follows: in Section II we outline the theoretical treatment of SBS including the key expressions, in Section III we describe the formulation's implementation, and in Section IV we present simulation examples which may serve as standard reference SBS calculations. In Appendix A we present the FEM formulation applied to the problem of solving for the elastic modes of a waveguide.

II. APPROACH OUTLINE

To study Brillouin scattering we require descriptions of optical and elastic propagation and the interaction between both fields. We consider the class of waveguide problems where both families of waves propagate along a common axis z and are, at least weakly, confined within the plane perpendicular to this axis. In this case the calculation of the Brillouin scattering interaction involves three main steps:

1) solving for the optical modes (fields and wavevectors) of the waveguide at a given frequency,
2) solving for the elastic modes (fields and frequencies) of the waveguide at a given wavevector (generally set according to the wavevector difference of the chosen optical modes),
3) evaluating the overlap integrals of the optical and elastic modal fields that describe the interaction between the fields.

The approach taken by our algorithm is to allow the user to specify the two optical modes, and then compute the relevant elastic mode from phase-matching requirements (see Section III-B). This approach maximizes the flexibility of the computation: the optical modes may be co- or counter-propagating, of different polarizations or mode order, or may differ significantly in frequency.

The geometry that we consider is a z-invariant waveguide capable of supporting both optical and acoustic waveguide modes. The electromagnetic properties of such a structure are described by the relative permittivity $\varepsilon_r(x, y)$, with the acoustic properties given by the components of the fourth rank stiffness tensor $c_{ijkl}(x, y)$ and the density $\rho(x, y)$ (see appendix B). The coupling between optical and acoustic waves depends on the photoelastic/electrostrictive effect, described by the symmetric fourth rank photoelastic (or Pockel's) tensor $p_{ijkl}(x, y)$. All elastic properties are defined across the cross-section of the waveguide; a vacuum condition (for an ideal suspended waveguide) can be modeled by imposing stress-free boundary conditions (see appendix B).

For the guided electromagnetic modes, each constituent mode, labeled n, of the pump (p) and Stokes (s) waves is taken to be of the form

$$\mathbf{E}_n^{(\mathrm{p,s})}(\mathbf{r}, t) = \mathbf{e}_n^{(\mathrm{p,s})}(x, y) \exp(ik_n^{(\mathrm{p,s})}z - i\omega_n^{(\mathrm{p,s})}t) + \text{c.c.}, \tag{1}$$

$$\mathbf{H}_n^{(\mathrm{p,s})}(\mathbf{r}, t) = \mathbf{h}_n^{(\mathrm{p,s})}(x, y) \exp(ik_n^{(\mathrm{p,s})}z - i\omega_n^{(\mathrm{p,s})}t) + \text{c.c.}, \tag{2}$$

where $\mathbf{e}_n^{(\mathrm{p,s})}(x, y)$ and $\mathbf{h}_n^{(\mathrm{p,s})}(x, y)$ are the electric and magnetic parts of the modal field distribution, $k_n^{(\mathrm{p,s})}$ is the propagation constant in the positive z-direction, $\omega_n^{(\mathrm{p,s})}$ is the optical angular frequency, t is time and c.c. represents the complex conjugate. Each constituent mode of the elastic wave, labeled m, is taken to be of the form

$$\mathbf{U}_m(\mathbf{r}, t) = \mathbf{u}_m(x, y) \exp(iq_m z - i\Omega_m t) + \text{c.c.}, \tag{3}$$

where $\mathbf{u}_m(x, y)$ is the modal field distribution of the elastic displacement, q_m is the propagation constant in the positive z-direction and Ω_m is the elastic angular frequency. We emphasize

that these modes are all fully vectorial, and include the longitudinal components e_z, h_z and u_z.

A. Modal Solutions

The electromagnetic modes are solutions to the vector Helmholtz equation which follows from Maxwell's equations. Specifically, we solve the Helmholtz equation in the form

$$-\nabla \times (\nabla \times \mathbf{E}) + \omega^2 \varepsilon_0 \varepsilon_r \mathbf{E} = \mathbf{0} \qquad (4)$$

with the $\mathbf{h}$ field found from Faraday's law.

The elastic modes are solutions to the elastic wave equation

$$\nabla \cdot \mathbf{T} + \Omega^2 \rho \, \mathbf{u} = \mathbf{0}. \qquad (5)$$

Here $\mathbf{T}$ is the elastic stress tensor, which is related to the linear strain tensor $\mathbf{S}$ by Hooke's law $\mathbf{T} = \mathbf{c} : \mathbf{S}$. Here $\mathbf{c}$ is the spatially-varying fourth rank stiffness tensor which describes the elastic material properties of the waveguide. A fuller presentation of the relevant elastic theory and our approach to constructing a finite element formulation is provided in appendix A.

B. Modal Properties

The power in Watts carried in each optical mode n is

$$P_n^{(p,s)} = 2\mathrm{Re} \int d^2r \, \hat{z} \cdot (\mathbf{e}_n^{(p,s)*} \times \mathbf{h}_n^{(p,s)}), \qquad (6)$$

where the integration is over the whole transverse plane. The corresponding linear energy density of the optical mode in units J·m^{-1} is

$$\mathcal{E}_n^{(p,s)} = 2\varepsilon_0 \int d^2r \, \varepsilon_r(x,y) \, \|\mathbf{e}_n\|^2, \qquad (7)$$

where ε_r is the (position-dependent) relative dielectric constant and ε_0 is the vacuum permittivity.

The linear density of elastic energy in units $J \cdot m^{-1}$ for the elastic modes is given by [16]

$$\mathcal{E}_m^{(a)} = 2\Omega^2 \int_A d^2r \, \rho \|\mathbf{u}\|^2, \qquad (8)$$

where the integration is strictly over the cross section of the waveguide, which is treated as being surrounded by vacuum. The corresponding modal elastic power is

$$P_m^{(a)} = \mathrm{Re} \int_A d^2r \, (-2i\Omega) \sum_{jkl} c_{zjkl} u_{mj}^* \partial_k u_{ml}, \qquad (9)$$

where c_{ijkl} is the position-dependent stiffness tensor of the waveguide. Note that following [10], we do not normalize the energy in each mode, instead carrying the energy terms through to the gain calculation in Eq. (12).

While in practice one must typically consider the SBS gain contributions of many elastic modes, as well as potentially different optical modes, in the interest of clarity we proceed with the treatment of an individual set of modes (one pump, one Stokes, one elastic), omitting the mode index subscripts and leaving the generalization to Section III.

The SBS gain of a particular combination of pump, Stokes and elastic modes is calculated as follows:

1) *Calculate the photoelastic (PE) interaction strength, which is the inverse process to electrostriction.* This is given in Eq. (33) in [10],

$$Q^{PE} = -\varepsilon_0 \int_A d^2\mathbf{r} \sum_{ijkl} \varepsilon_r^2 e_i^{(s)*} e_j^{(p)} p_{ijkl} \partial_k u_l^*, \qquad (10)$$

where Q^{PE} is the photoelastic coupling in units $W \cdot m^{-1} \cdot s$ and p_{ijkl} is the dimensionless photoelastic tensor.[2]

2) *Calculate the moving boundary (MB) interaction, which is the inverse phenomenon to radiation pressure.* This coupling, measured in units $W \cdot m^{-1} \cdot s$, is given by [2]

$$Q^{MB} = \int_{\mathcal{C}} d\mathbf{r} \, (\mathbf{u}^* \cdot \hat{n})$$
$$\times \left[(\varepsilon_a - \varepsilon_b)\varepsilon_0 (\hat{n} \times \mathbf{e}^{(s)})^* \cdot (\hat{n} \times \mathbf{e}^{(p)}) \right.$$
$$\left. - (\varepsilon_a^{-1} - \varepsilon_b^{-1})\varepsilon_0^{-1} (\hat{n} \cdot \mathbf{d}^{(s)})^* \cdot (\hat{n} \cdot \mathbf{d}^{(p)}) \right], \qquad (11)$$

where the integral is taken in the positive sense with respect to the outward normal around the contour of the waveguide boundary $\mathcal{C}$.[3]

3) *Finally, calculate the SBS gain.* The peak SBS gain, Γ_0, in units $W^{-1} \cdot m^{-1}$ of this particular combination of pump, Stokes and elastic modes is given by Eq. (91) in [10],

$$\Gamma_0 = \frac{2\omega\Omega}{\alpha} \frac{(|Q^{Tot}|^2)}{P^{(s)} P^{(p)} \mathcal{E}^{(a)}}, \qquad (12)$$

where

$$Q^{Tot} = Q^{PE} + Q^{MB}, \qquad (13)$$

α is the temporal elastic attenuation coefficient in units s^{-1}, and ω is chosen to be $\omega^{(p)}$, which typically varies from $\omega^{(s)}$ by less than 0.01%. We note that, in contrast to [10], we normalize with the elastic energy (Eq. (8) and Eq. (16) in [10]) rather than elastic power (Eq. (18) in [10]). This choice was made to better handle forward SBS, where the power flow associated with transverse elastic oscillations is near zero while the energy density remains finite. We also note that because the modal powers are defined in accordance with the direction of energy carried (negative power for a backward-propagating wave) the SBS gain arising from Eq. (12) will be positive for co-propagating interactions, and negative for counter-propagating or backward SBS. The gain driven by solely the photoelastic or radiation pressure effects is given by Eq. (12) with $Q^{Tot} = Q^{PE}$ or $Q^{Tot} = Q^{MB}$ respectively. We note also that Q^{PE} and MB are signed quantities, allowing consideration of SBS cancellation effects [15] as discussed below.

The elastic attenuation due to dissipation can be derived by considering the propagating of an elastic mode in a waveguide possessing a non-zero viscosity tensor (see p. 143

---

[2]Note that here we have corrected a sign error in Eq. (31) and (33) of [10], so that the photoelastic tensor here matches the standard convention that the electric susceptibility is $\chi_{ij}^{PE} = -\varepsilon_r^2 \sum_{kl} p_{ijkl} \partial_k u_l$.

[3]There is a sign error in Eq. (41) in [10], which is corrected here by the replacement $(\varepsilon_b^{-1} - \varepsilon_a^{-1}) \mapsto (\varepsilon_a^{-1} - \varepsilon_b^{-1})$.

in [18]). In terms of the visco-elastic tensor η_{ijkl} and the deformation, the loss per unit time (i.e., in units s^{-1}) of the elastic amplitude is

$$\alpha = \frac{\Omega^2}{\mathcal{E}^{(a)}} \int_A \mathrm{d}^2 r \sum_{ijkl} \partial_i u_j^* \eta_{ijkl} \partial_k u_l . \qquad (14)$$

We note that a similar expression given in Eq. (45) in [10] neglects contributions from the boundaries when performing an integration by parts of Eq. (14).

Further attenuation occurs due to scattering and radiation losses. We do not here present theoretical expressions for these losses, but their contributions can be included by calculating α based on an assumed quality factor Q_{loss}, which may be estimated from experimental measurements. In such a case, we set

$$\alpha = \frac{v_g q}{2 Q_{\mathrm{loss}}}, \qquad (15)$$

where v_g is the group velocity of the elastic mode. If, for example, the frequency and spectral linewidth of a mode's SBS resonance is known, then $Q_{\mathrm{loss}} = \Omega_0/(2\pi\gamma)$, where Ω_0 is the central angular frequency, and γ is the spectral linewidth with respect to angular frequency in units s^{-1}. It is often of interest to plot the SBS gain profile in frequency, including the contributions from multiple modes. To facilitate this, we assume each resonance to be Lorentzian with the linewidth $\gamma = \alpha/2\pi$,

$$\Gamma(\delta\Omega) = \Gamma_0 \frac{(\gamma/2)^2}{(\gamma/2)^2 + (\delta\Omega)^2}, \qquad (16)$$

where $\delta\Omega$ is the range of angular frequency detuning.

Having established the fundamentals of the theoretical formulation, we now describe the specifics of the implementation of the algorithm.

III. COMPUTATIONAL IMPLEMENTATION

Our approach, available online at [5], is implemented using a combination of Fortran and Python. Fortran is chosen for the numerically intensive subroutines because of its numerical efficiency and access to extensively optimized open source linear algebra packages including BLAS, LAPACK and UMF-PACK [19]. Python is used for the remainder of the program, providing full access to all variables, and thereby facilitating both high level parameter sweeps and low level manipulation of basic field quantities. The communication between subroutines written in each language is handled by the f2py package [20], which creates a Python wrapper around the Fortran source code, with pointers to memory blocks being passed directly to Python creating minimal computational overhead. In this way we balance the need for efficient numerical computation and ease of use.

The optical modes are computed in the frequency domain, so that each frequency is independent and problems that span across wavelength ranges are 'embarrassingly parallel'. This means that the calculation at each wavelength may run in parallel on separate CPUs without any communication between them. This

is done in Python using the `multiprocessing` package. To minimize the computational overhead and thereby maximize the speed enhancement of parallelization we do not introduce any parallel elements to the calculation for each wavelength, though users may use parallel versions of the linear algebra packages. Calculations across structural parameters are also trivially parallelized, and the script file approach is particularly well suited to setting up a scan of multiple parameters to be carried out in parallel.

To illustrate the algorithm we present an example simulation shown in Figs. 1–4.

A. Setup

Figures 1–4 show a basic NumBAT control script. As seen in Fig. 1, a simulation begins with the specification of the optical wavelength and the waveguide's geometry and constituent materials. In the example of Fig. 1, the optical wavelength is set in line 13, the key parameters of the waveguide are defined in lines 14–18 (the prefix `inc` stands for "inclusion"), and the waveguide object is initialized in lines 34–37 where the FEM mesh is created using the open-source program Gmsh [21]. In lines 21–31 we specify the desired number of modes, and which combinations of these modes will be included in the gain calculations.

In this example simulation we consider backward SBS, with the pump and Stokes waves both occupying the fundamental mode of the waveguide. In this case we seek results for the first ten eigenmodes, and specify the minimum number of modes in the ARPACK [22]. expansion required for stability at twice this number with `num_modes_EM_pump = 20`. We then specify that only the modal combinations including the fundamental mode `EM_ival_pump = 0`, `EM_ival_stokes = 0` need to be considered in the calculation of the gain, which saves considerable computation time. For the same reason, the number of elastic modes must also be at least 20. Values greater than this are recommended when a wide gain spectrum is desired.

B. Modal Fields

To initialize the search for the modes of the waveguide we must supply the FEM modesolver with an estimate of the wavevector of the target mode, which is most conveniently achieved by estimating the mode's effective index (`n_eff`). In the example simulation, we are interested in the fundamental mode and estimate its effective index as being slightly less than the refractive index of the waveguide material (Fig. 3, line 40). The mode solver is relatively insensitive to this initial estimate. Calculating the optical modes of the pump wave is then a simple one line call (Fig. 3, line 42), which returns a Python object that contains the wavevectors (eigenvalues), fields (eigenvectors), and optical power (as per Eq. (6)) of each mode.

In the example we consider a simplified backward SBS computation, in which we observe that the difference in frequency between pump and Stokes is sufficiently small, and the optical dispersion sufficiently low, that the Stokes modes are essentially identical to backward-propagating pump modes. In this calculation the `mode_calcs.bkwd_`

```
1: import numpy as np
2: import sys
3: sys.path.append("../backend/")
4:
5: import materials
6: import objects
7: import mode_calcs
8: import integration
9: import plotting
10: from fortran import NumBAT
11:
12: # Geometric parameters in nanometers.
13: wl_nm = 1550   # Wavelength of EM wave in vacuum.
14: unitcell_x = 2.5*wl_nm   # Large unit cell to ensure fields zero at boundary.
15: unitcell_y = unitcell_x
16: inc_a_x = 300   # Waveguide width.
17: inc_a_y = 280   # Waveguide height.
18: inc_shape = 'rectangular'   # Shape of waveguide.
19:
20: # Number of electromagnetic modes to solve for.
21: num_modes_EM_pump = 20
22: num_modes_EM_Stokes = num_modes_EM_pump
23: # Number of acoustic modes to solve for.
24: num_modes_AC = 20
25: # The first EM mode(s) for which to calculate interaction with AC modes.
26: # Can specify a mode number (zero has lowest propagation constant) or 'All'.
27: EM_ival_pump = 0
28: # The second EM mode(s) for which to calculate interaction with AC modes.
29: EM_ival_Stokes = EM_ival_pump
30: # The AC mode(s) for which to calculate interaction with EM modes.
31: AC_ival = 'All'
32:
33: # Use specified parameters to create a waveguide object.
34: wguide = objects.Struct(unitcell_x,inc_a_x,unitcell_y,inc_a_y,inc_shape,
35:                         material_a=materials.Vacuum,
36:                         material_b=materials.Si_2016_Smith,
37:                         lc_bkg=2, lc2=200.0, lc3=5.0)
```

Fig. 1.   Example simulation part 1/3, showing the specification of parameters and the initialization of the waveguide object.
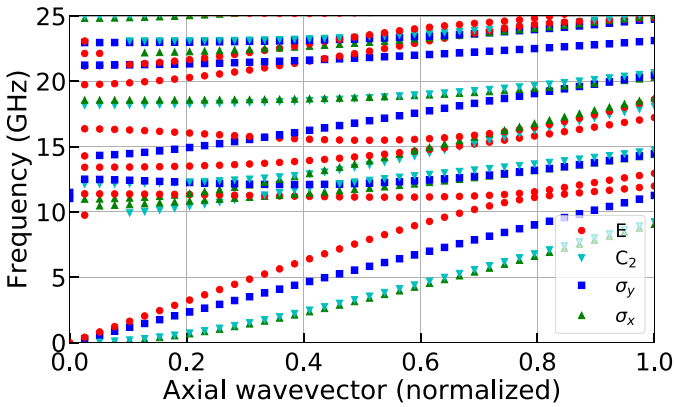

Fig. 2.   Elastic dispersion relation for a geometry similar to that in Ref. [2], included as Tutorial 3 in the NumBAT documentation. The structure is a rectangular silicon waveguide of dimensions 314.7 nm by 283.2 nm. The different colours allow identification of elastic modes of different symmetry, as indicated in the inset legend.

`Stokes_modes(sim_EM_pump)` routine transforms the pump modes, reversing the direction of a mode by conjugating its fields and reversing the wavevector.

In all cases, the wavevector of the elastic modes is equal to the difference in wavevectors of the pump and Stokes waves (Fig. 3 line 50)

$$q = k^{(p)} - k^{(s)}. \tag{17}$$

In the call to `wguide.calc_AC_modes` in line 52, the elastic FEM modesolver takes this wavevector q as an input and returns the frequencies Ω_m of the elastic modes. (Note that this is a reverse procedure to that of the optical modesolver which solves for the wavevectors k for given frequency ω). The other key input into the elastic FEM is a modified version of the FEM mesh, where any regions representing vacuum have been removed. This is generally best done by passing through the Python object that contains the results of the optical simulation as the argument `sim_EM=sim_EM_pump`, in which case NumBAT handles the conversion. If users wish to compute just the elastic modal properties of the waveguide, they can create a FEM mesh that covers the waveguide cross-section, and leave out the keyword argument `sim_EM`. The FEM modesolver also requires an initial estimate of where to start its search, which in the elastic case is by default estimated in the `calc_AC_modes` routine, based on the group velocity of a longitudinal mode in bulk. The estimate of the lowest frequency of interest can be set using the keyword argument `shift_Hz`. The calculation of the elastic modes is a simple one line call (Fig. 3 line 52), which returns a Python object that contains the frequencies (eigenvalues), fields (eigenvectors), and energy density (as per Eq. (8))

```
39: # Expected effective index of fundamental guided mode.
40: n_eff = wguide.material_b.n-0.1
41: # Calculate the EM modes of the pump field.
42: sim_EM_pump = wguide.calc_EM_modes(num_modes_EM_pump, wl_nm, n_eff)
43: # Print the wavevectors of EM modes.
44: print('\n k_z of EM modes \n', np.round(np.real(sim_EM_pump.Eig_values),4))
45: # For an idealised backward SBS simulation the Stokes modes are identical
46: # to the pump modes but travel in the opposite direction.
47: sim_EM_Stokes = mode_calcs.bkwd_Stokes_modes(sim_EM_pump)
48:
49: # Acoustic wavevector
50: k_AC = np.real(sim_EM_pump.Eig_values[0] - sim_EM_Stokes.Eig_values[0])
51: # Calculate acoustic modes, using the mesh from the EM calculation.
52: sim_AC = wguide.calc_AC_modes(num_modes_AC, k_AC, EM_sim=sim_EM_pump)
53: # Print the frequencies of AC modes.
54: print('\n Freqs of AC modes (GHz) \n', np.round(np.real(sim_AC.Eig_values)*1e-9, 4))
55:
56: # Calculate total SBS gain, SBS gain for PE and MB effects individually,
57: # as well as acoustic loss and quality factor.
58: SBS_gain, SBS_gain_PE, SBS_gain_MB,linewidth_Hz, Q_factors, alpha = integration.gain_and_q(
59:     sim_EM_pump, sim_EM_Stokes, sim_AC, k_AC,
60:     EM_ival_pump=EM_ival_pump, EM_ival_Stokes=EM_ival_Stokes, AC_ival=AC_ival)
61: # Print the Backward SBS gain of the AC modes.
62: print("\n SBS_gain PE contribution \n", SBS_gain_PE[EM_ival_Stokes,EM_ival_pump,:])
63: print("SBS_gain MB contribution \n", SBS_gain_MB[EM_ival_Stokes,EM_ival_pump,:])
64: print("SBS_gain total \n", SBS_gain[EM_ival_Stokes,EM_ival_pump])
```

Fig. 3.   Example simulation part 2/3, showing the calculation of the optical and elastic modes as well as the SBS gain.

```
66: # Plot modal fields
67: plotting.plt_mode_fields(sim_EM_pump, EM_AC='EM_E')
68: plotting.plt_mode_fields(sim_AC, EM_AC='AC')
69:
70: # Construct the SBS gain spectrum.
71: freq_min = 10   # GHz
72: freq_max = 25   # GHz
73: plotting.gain_specta(sim_AC, SBS_gain, SBS_gain_PE, SBS_gain_MB, linewidth_Hz, k_AC,
74:     EM_ival_pump, EM_ival_Stokes, AC_ival, freq_min=freq_min, freq_max=freq_max)
```

Fig. 4.   Example simulation part 3/3, showing the plotting of modal fields and SBS gain spectrum.

of each mode. Figure 2 shows a calculated dispersion relation for the elastic modes for a geometry similar to a rectangular waveguide studied in Ref. [2]. The figure illustrates that where possible NumBAT classifies the elastic modes by their symmetry class, which allows quick identification of modes that will yield a nonzero coupling between the desired optical modes [4].

We note that solving the eigensystems to find the optical and elastic modes is by far the most computationally expensive step in NumBAT and that at the completion of these steps the SBS problem is now reduced to numerical quadrature.

C. SBS Interactions

The SBS gain may now be found by evaluating the SBS (photoelastic and moving boundary) interaction as described in the integrals of Eqs. (10)–(12). This is done using the integration.gain_and_qs function as shown in lines 58–61 of Fig. 3. This function returns the total peak SBS gain ($Q^{\text{Tot}} = Q^{\text{PE}} + Q^{\text{MB}}$, SBS_gain), as well as the peak SBS gain due solely to the photoelastic ($Q^{\text{Tot}} = Q^{\text{PE}}$, SBS_gain_PE) and moving boundary ($Q^{\text{Tot}} = Q^{\text{MB}}$, SBS_gain_MB) effects. The function integration.gain_and_qs also evaluates the elastic loss as per Eq. (14), unless predetermined quality factors are input using the fixed_Q keyword argument, in which case α is set as per Eq. (15).

The evaluation of these integrals for all combinations of optical and elastic modes is relatively computationally intensive and they are therefore implemented in NumBAT using Fortran subroutines. The surface integrals of the photoelastic interaction and the elastic loss (Eqs. (10) and (14), respectively) have been implemented twice: once using a semi-analytical approach that is valid on rectilinear triangles (the integral over each triangle is computed analytically,) and may therefore be applied on purely rectangular structures, while the second subroutines use numerical quadrature over each triangle and can therefore be applied on any mesh, including ones that contain curvi-linear triangles. The (one-dimensional) contour integral of Eq. (11) (moving boundary effect) is also implemented in a Fortran subroutine. This subroutine identifies elements that form the boundary between different materials, orientates the edges of these mesh elements consistently to form a contour, and then evaluates the integral using numerical quadrature.

D. Plotting Fields and Gains

Lastly, we plot the fields of the optical and elastic modes as well as the SBS gain spectrum. This is done in lines 67, 68 and 71–74 of Fig. 4. The gain spectrum is the superposition of the Lorentzian resonances of each combination of the optical and elastic modes, calculated using Eq. (16). The plotting.gain_spectra function generates a plot of the gain

spectrum due to the photoelastic effect, the gain spectrum due to the moving boundary effect, and the total gain spectrum (as shown for example in Fig. 8). The same function can be instructed to plot the Lorentzian gain curves of each combination of individual optical and acoustic modes.

IV. STANDARD BENCHMARKS

A central motivation of this paper is to create a set of open source reference studies that the research community can use to benchmark other software. For such a database to be trustworthy it is crucial that all information is freely available so it may be scrutinized and replicated. This includes all geometric and material parameters, the theoretical formulation and numerical implementation of the simulation, and the full suite of calculation results. While we cannot include all of this data in this paper, this section contains a selection of our suggested benchmark studies, including their defining parameters and the solutions as calculated by our algorithm. Further reference examples and full data are contained in NumBAT's online repository [5].

Here we present four reference examples that cover backward SBS, forward intramodal SBS and forward intermodal SBS, in various waveguide geometries and materials that are included in the NumBAT suite of literature examples. Each reference case has reliable published experimental results:

- Forward intramodal SBS in a rectangular silicon waveguide, as studied by Van Laer *et al.* [23]
- Backward SBS self-cancellation in a silica nanowire, as studied by Florez *et al.* [15]
- Forward SBS in a silicon rib waveguide, as studied by Kittlaus *et al.* [24]
- Backward SBS in a chalcogenide rib waveguide, as studied by Morrison *et al.* [25]

Note that a convergence study for one problem is included in Appendix A.

A. Benchmark 1: Forward Intramodal SBS in a Rectangular Silicon Waveguide (NumBAT Literature Example 3.6.4)

We chose to replicate the results in [23] as an experimental demonstration of forward intramodal SBS. While the fabricated sample of [23] has the rectangular silicon waveguide supported by a nanoscale pedestal, here we make the simplification that it is suspended in air as illustrated in Fig. 5. This makes for a better canonical reference case and brings the example in line with the original structures proposed for "giant SBS" in nanophotonic waveguides [2]. In our calculation, the waveguide has a rectangular cross-section (see Fig. 5), with side lengths $a = 485$ nm and $b = 230$ nm. Note that we have increased the width by 10% from the values in [23] to accommodate for the bulging shape of the fabricated sample.

NumBAT's online repository [5] also contains a related example with the pedestal included; the elastic leakage through the pedestal is however not yet handled in the current version of NumBAT, which will require the addition of a surrounding elastic perfectly matched layer.
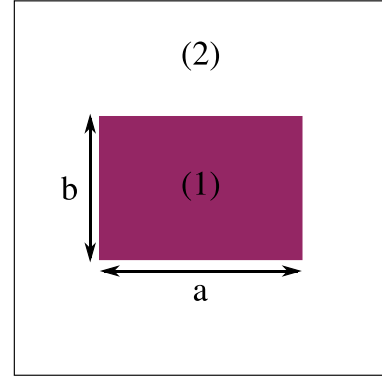

Fig. 5. Cross-section of a rectangular silicon waveguide (1) surrounded by air (2).
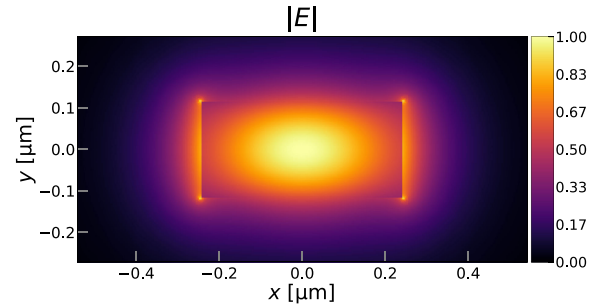

Fig. 6. Fundamental optical mode profile for the problem in Benchmark 1. The dominant electric field component is in the x-direction.

For silicon we use the material properties from [26]: a refractive index of 3.48; a density of 2329 kg/m^3; stiffness tensor components of $c_{11} = 165.6$ GPa, $c_{12} = 63.9$ GPa, $c_{44} = 79.5$ GPa; photoelastic tensor components of $p_{11} = -0.094$, $p_{12} = 0.017$, $p_{44} = -0.051$; and elastic loss tensor components of $\eta_{11} = 0.0059$ Pa · s, $\eta_{12} = 0.00516$ Pa · s, $\eta_{44} = 0.00062$ Pa · s. These reference values are for silicon with $\langle 100 \rangle$ crystalline orientation, whereas the experiment is for $\langle 110 \rangle$ silicon, so we use NumBAT's inbuilt function `rotate_tensor` to rotate the (fourth rank) tensors appropriately [18].

The amplitude $|\mathbf{E}|$ profile of the fundamental optical mode, at the wavelength $\lambda = 1550$ nm, is shown in Fig. 6, and the profiles of the elastic mode components are shown in Fig. 7. Note that our method ignores air regions for elastic calculations, i.e. treating the air as vacuum, so elastic mode plots (eg. Fig. 7) only show data in regions of non-air materials.

The forward SBS gain Γ is shown in Fig. 8 and is in good agreement with the experimental result of Fig. 2a of [23], with a clear peak near 9.2 GHz. In Fig. 8, the legends "PE", "MB" and "Total" correspond respectively to the gain due to the photoelastic effect Q^{PE} (see Eq. (10)) alone, the gain due to moving boundary effect Q^{MB} (see Eq. (11)) alone, and the total gain Q^{Tot} (see Eq. (13)). The peak gain in the spectrum is 2907 W^{-1} · m^{-1}, which is close to the experimental value of 3200 W^{-1} · m^{-1}. The minor discrepancy in frequency and gain is due to the non-square shape of the fabricated sample, the
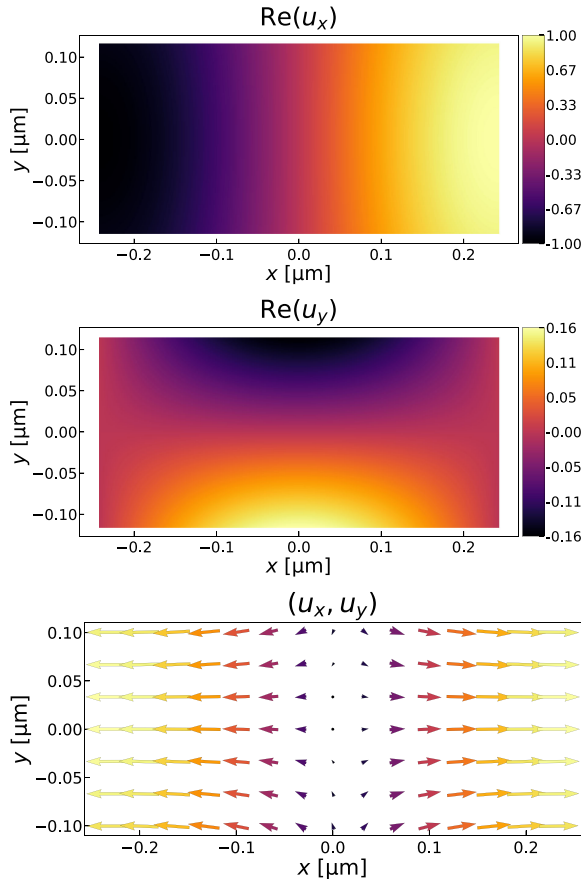
Fig. 7. Field components u_x and u_y and vector plot of the transverse field (u_x, u_y) of the elastic mode at 9.23 GHz for the problem in Benchmark 1. (The imaginary parts of these components are zero.)
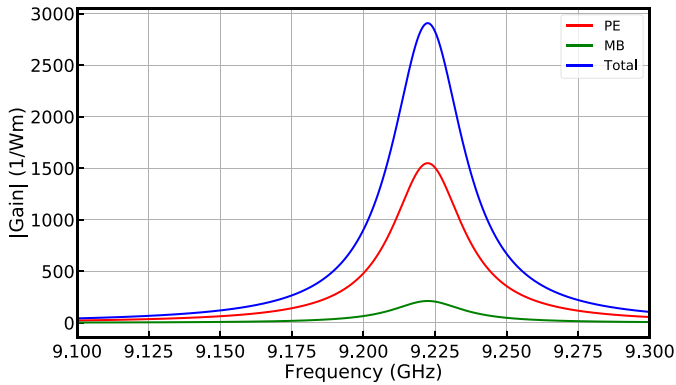

Fig. 8. Gain spectrum for the problem in Benchmark 1, equivalent to Fig. 2a in [23]. The minor difference in center frequency compared with the paper is due to the non-square shape of the fabricated sample as well as the supporting pedestal.

supporting pedestal, as well as minor differences in material properties.[4] Observe that the peak values satisfy the relation $\Gamma^{\text{Total}} = (\sqrt{\Gamma^{\text{PE}}} + \sqrt{\Gamma^{\text{MB}}})^2$.
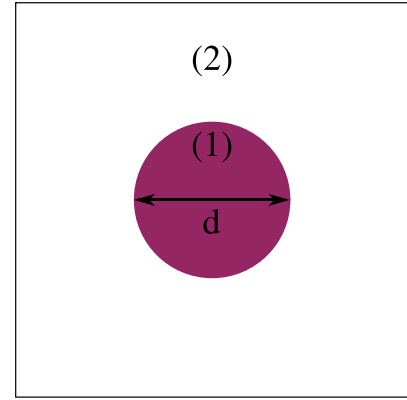
[4]See supplementary materials of [23].

Fig. 9. Cross-section of a circular wire (1) surrounded by air (2).

B. Benchmark 2: SBS Self-Cancellation in a Silica Nanowire (NumBAT Literature Example 3.6.6)

It is possible to design waveguides such that the gain components Q^{PE} and Q^{MB} satisfy $Q^{\text{PE}} = -Q^{\text{MB}}$, which causes the cancellation of the total gain $Q^{\text{Tot}} = Q^{\text{PE}} + Q^{\text{MB}}$. This phenomenon provides an excellent numerical test because any error in the sign or magnitude of the radiation pressure or moving boundary terms will be readily apparent in the absence of the cancellation. This Brillouin scattering self-cancellation effect was first demonstrated by Florez *et al.* [15], whose structure we reproduce here.

As illustrated in Fig. 9, the waveguide is a silica nanowire with a circular cross-section of diameter d (refractive index n_1), surrounded by air (refractive index n_2). For silica we use the material properties from [11]: a refractive index of 1.44; a density of 2203 kg/m^3; stiffness tensor components of $c_{11} = 78$ GPa, $c_{12} = 16$ GPa, $c_{44} = 31$ GPa; photoelastic tensor components of $p_{11} = 0.12$, $p_{12} = 0.270$, $p_{44} = -0.073$; and elastic loss tensor components of $\eta_{11} = 0.0016$ Pa $\cdot$ s, $\eta_{12} = 0.00129$ Pa $\cdot$ s, $\eta_{44} = 0.00016$ Pa $\cdot$ s. The wavelength of the incident optical wave is $\lambda = 1550$ nm.

For a nanowire of diameter $d = 550$ nm, the magnitude $|\mathbf{u}|$ and the transverse displacement field (u_x, u_y), of the two lowest order elastic modes, are plotted in Fig. 10(a) and (b). The transverse components of the modes in the panels (a) and (b) of Fig. 10 have respectively an axially asymmetric torsional-radial profile (TR$_{21}$ mode) and an axially symmetric radial profile (R$_{01}$ mode).

In Fig. 10(b), although the transverse displacement field of the R$_{01}$ mode has small values near the waveguide center, we observe that the total magnitude $|\mathbf{u}|$ of the R$_{01}$ mode is large near the center. This is due to the fact that the longitudinal displacement u_z takes large values near the waveguide center, which is consistent with the curves in Fig. 5a of [15].

The total gain spectrum of the silica nanowire with a diameter 550 nm is shown in blue in Fig. 11 and matches the blue curve of Fig. 3b in [15]. Both the TR$_{21}$ mode (elastic frequency 5.88 GHz) and the R$_{01}$ mode (elastic frequency 6.30 GHz) display a significant total gain in Fig. 11. As observed in [15], the total gain of the TR$_{21}$ mode is dominated by the contribution from the photoelastic effect, while both the photoelastic effect
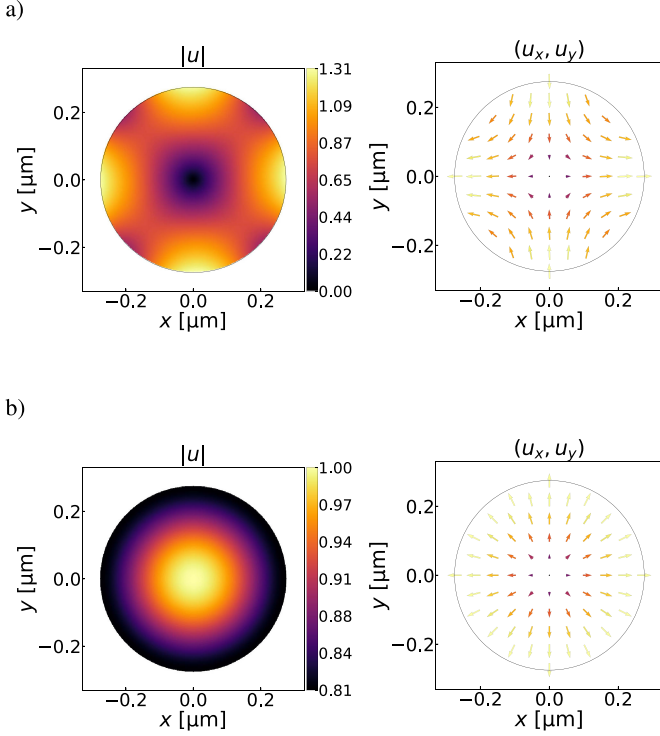
a)

b)

Fig. 10. Mode profiles of the two lowest order elastic modes of a silica nanowire with a diameter $d = 550$ nm for Benchmark 2 (see also Fig. 2(a, b) in Florez *et al.* [15]). The elastic frequency of the modes in (a) and (b) are respectively 5.88 GHz (R_{01}) and 6.30 GHz (TR_{21}).
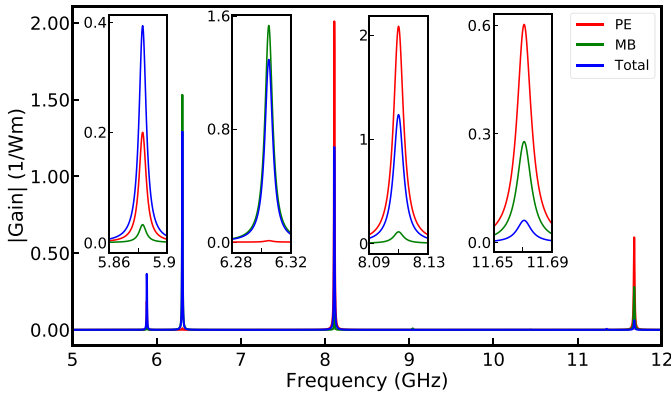

Fig. 11. Gain spectra of a silica nanowire with diameter 550 nm for Benchmark 2, matching the blue curve of Fig. 3b in Florez *et al.* [15]. The insets show the same data in the vicinity of the four peaks.

and the moving boundary effect can play a significant role in the total gain of the R_{01} mode. In particular, when the diameter of the nanowire is $d = 1160$ nm, for the R_{01} mode, the contributions from the photoelastic effect and moving boundary effect are equal and opposite, resulting in a Brillouin scattering self-cancellation. This is confirmed by the gain spectrum in Fig. 12, which shows near perfect cancellation at 5.4 GHz. For clarity, the curves in Fig. 12 are shown on a log-scale in Fig. 13, revealing that the cancellation holds to approximately one part in a thousand. The gain spectra in Figs. 12 and 13 are in agreement with the results in Fig. 4 of [15].
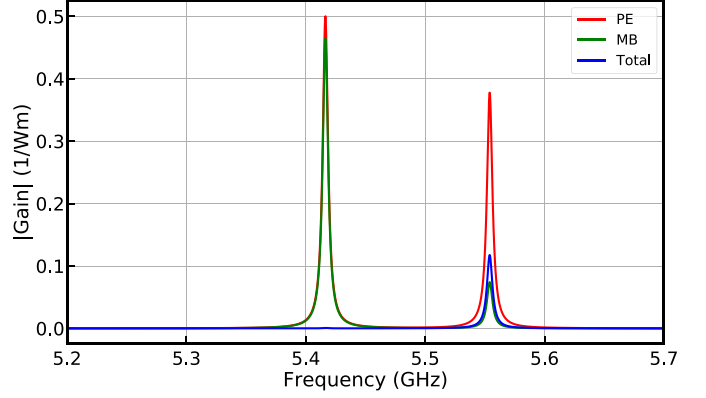

Fig. 12. Gain spectra of a silica nanowire with diameter $d = 1160$ nm for Benchmark 2, as in Fig. 4 of Florez *et al.* [15], showing near perfect cancellation at 5.4 GHz.
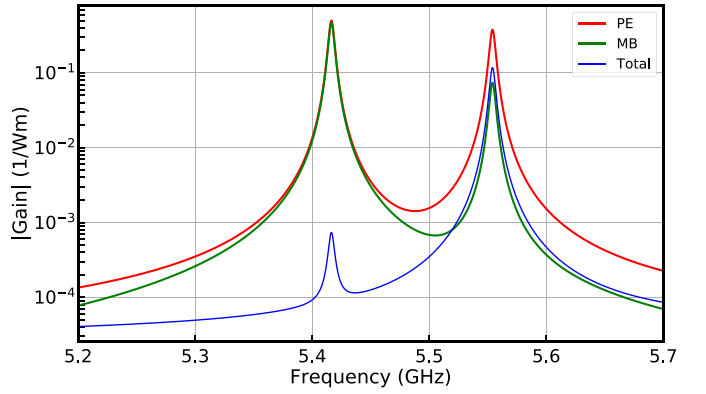

Fig. 13. The same gain spectra as in Fig. 12 plotted on a log-scale highlighting the gain cancellation at 5.4 GHz.

C. Benchmark 3: Forward Intermodal SBS in a Silicon Rib Waveguide (NumBAT Literature Example 3.6.8)

Next we simulate forward intermodal SBS in a silicon rib waveguide. This structure has been used in recent experiments by Kittlaus *et al.* [24] and consists of a ridge that is 80 nm high and 1500 nm wide upon a membrane that is 135 nm and 2850 nm wide. Note that Fig. 2e in [24] shows the height of the membrane to be 145 nm while the text describes the layer as being 135 nm thick; we use 135 nm here. Once again the crystalline orientation of silicon is $\langle 110 \rangle$ and the material properties are the same as in Section IV-A.

Figure 14 shows the fundamental optical mode fields of the structure, corresponding to Fig. 2f, g in [24]. Figure 15 shows the elastic mode fields of the modes at 6.27 GHz, 2.82 GHz, and 1.33 GHz, corresponding to Fig. 3c of [24].

Figure 16 shows the gain spectra equivalent to Fig. 3b in [24]. Note that the gain is completely dominated by the photoelastic effect—this is because the only non-canceling contribution from the moving boundaries comes from the small vertical sections at the side of the central rib, where both the optical and elastic intensities are extremely small.
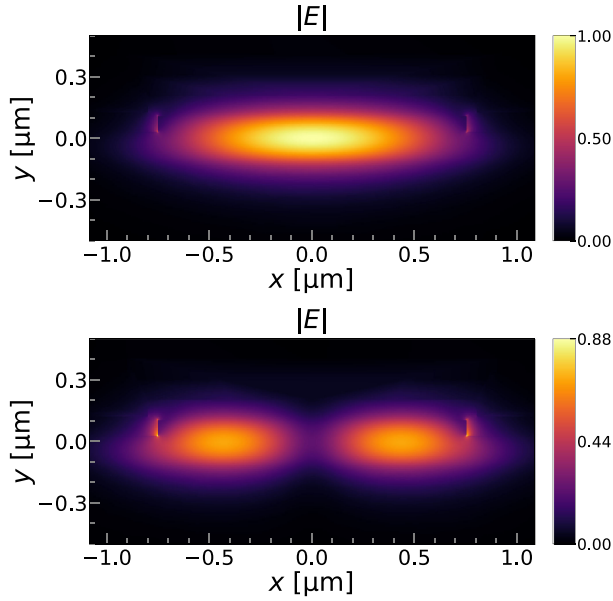
Fig. 14. Fundamental (a) and second order (b) optical mode fields of the Benchmark 3 structure of [24], equivalent to Fig. 2f, g in [24]. In each case, the dominant field component is E_x.
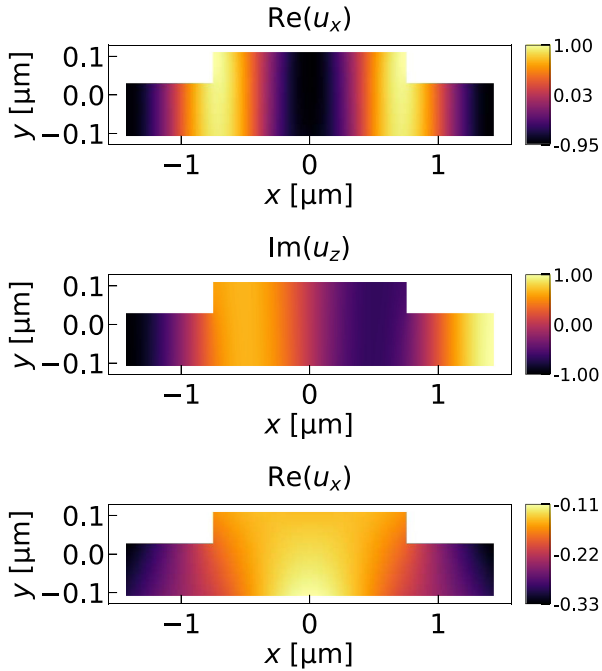

Fig. 15. Dominant components of high gain elastic modes for Benchmark 3 as shown in Fig. 3c of [24]. The elastic frequency of the modes from top to bottom are respectively 6.27 GHz, 2.82 GHz, and 1.33 GHz. The imaginary part of u_x and real part of u_z vanish in these cases.

D. Benchmark 4: Backward SBS in a Chalcogenide Rib Waveguide (NumBAT Literature Example 3.6.10)

Stimulated Brillouin scattering in integrated devices was first demonstrated in partially etched rib waveguides made of a soft amorphous glass, As_2S_3 [1]. The large photoelastic constants make strong Brillouin interactions possible in even large
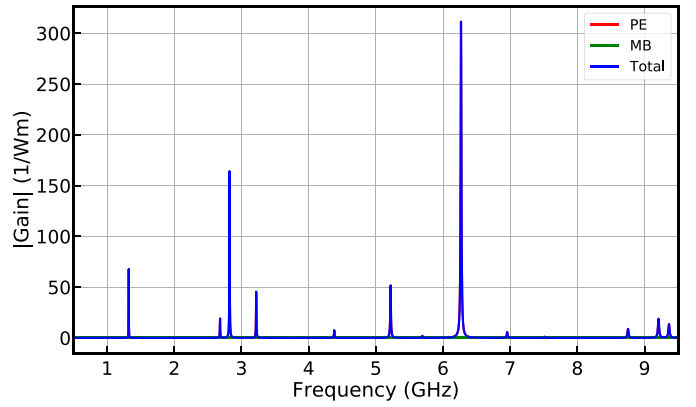

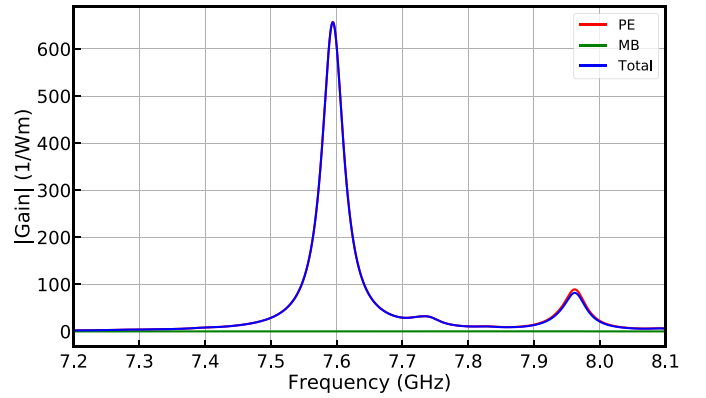Fig. 16. Gain spectra for Benchmark 3 equivalent to Fig. 3b in [24].

Fig. 17. Gain spectra for Benchmark 4 equivalent to Fig. 3c in [25].

mode area waveguides, with amplification factors beyond 50 dB being generated in certain structures [27]. Here we perform simulations of a recent experimental design from Morrison *et al.*: a fully etched As_2S_3 waveguide clad in SiO_2, formed within a wider Si circuit [25]. This result is a useful benchmark due to its distinctive frequency spectrum, comprising of multiple elastic modes with varying opto-elastic overlaps. Unlike the earlier examples, this particular waveguide geometry is highly multimoded for the elastic wave, with over 100 elastic modes needing to be accounted for when finding the SBS gain.

For As_2S_3 we use a refractive index of 2.44; a density of 3150 kg/m³; stiffness tensor components of $c_{11} = 19.75\,\mathrm{GPa}$, $c_{12} = 8.7\,\mathrm{GPa}$, $c_{44} = 5.525\,\mathrm{GPa}$; photoelastic tensor components of $p_{11} = 0.25$, $p_{12} = 0.23$, $p_{44} = 0.01$; and elastic loss tensor components of $\eta_{11} = 0.0018\,\mathrm{Pa \cdot s}$, $\eta_{12} = 0.00145\,\mathrm{Pa \cdot s}$, $\eta_{44} = 0.00018\,\mathrm{Pa \cdot s}$.

Figure 17 shows the gain spectra corresponding to Fig. 3c in [25] with a peak gain of 660 $\mathrm{W^{-1} \cdot m^{-1}}$, which is almost exclusively driven by the photoelastic effect due to the large cross section area of the waveguide. The experimentally measured gain from the example in Fig. 17 is $(750 \pm 50)\,\mathrm{W^{-1} \cdot m^{-1}}$, with the discrepancy attributed to uncertainties in the elastic loss tensor components.

V. CONCLUSION

Standardized tests are an essential component for the development of scientific software. We believe that this work will serve the needs of the optomechanics community by providing such a suite of tests, together with code that can be used both for investigations of the underlying physics of SBS as well as for the design of new Brillouin-active waveguide systems.

Several extensions of this work are envisaged and are in the process of implementation. The first is the inclusion of open boundaries for the elastic problem—this is important for a large number of experiments, in which the acoustic mode is not strictly confined but can radiate away from the waveguide core through the substrate. This process results in an additional component to elastic loss that dominates material losses. Such elastic radiation loss can be computed either perturbatively, from the magnitude of the elastic field components at some distance from the waveguide, or directly, through the imposition of an elastic perfectly-matched layer on the boundary of the computational domain. A second extension is the inclusion of roto-optic effects, which manifest in optically-anisotropic materials and structures, such as stacks of thin layers which differ in their elastic properties. Recent analysis [28] has shown that the Brillouin gain resulting from such structures can be significant, even dominating the photoelastic-induced gain which is accounted for here. It is a straightforward process to include this contribution within the framework of NumBAT.

A final extension is to the computation of gain in waveguides that are not longitudinally invariant, such as photonic crystal waveguides and rib-waveguides with periodic supporting struts. The computation of SBS gain in these structures requires an extension of the FEM routine to three-dimensional mode computations, taking into account the changed requirements of phase matching between modes which become more complicated in periodically-replicated media.

Note: at the time of submission, we became aware of very recent related work by Malinowski and Fathpour [29].

APPENDIX

As an example of our tool's convergence as a function of the resolution of the FEM mesh we study backward SBS in a rectangular silicon waveguide surrounded by vacuum. This simulation is included in the tutorial [5] as it is important to carry out convergence testing of this sort (as well as convergence against the number of modes included) whenever simulating new structures.

Figure 18(a) shows the convergence of the elastic frequency, and Fig. 18(b) shows the convergence of the SBS gain, both as a function of the mesh refinement parameter `lc_2`. This parameter sets the characteristic length of the FEM elements on the boundary of the waveguide as `lc_bkg / lc_2`, where `lc_bkg` is the background mesh size. The larger `lc_2` the finer the mesh on the waveguide boundary. In each figure we show only those modes that experience significant gain, representing the absolute value of the quantity in dashed lines with circular markers, and the error relative to the most finely resolved mesh in solid lines with triangular markers.
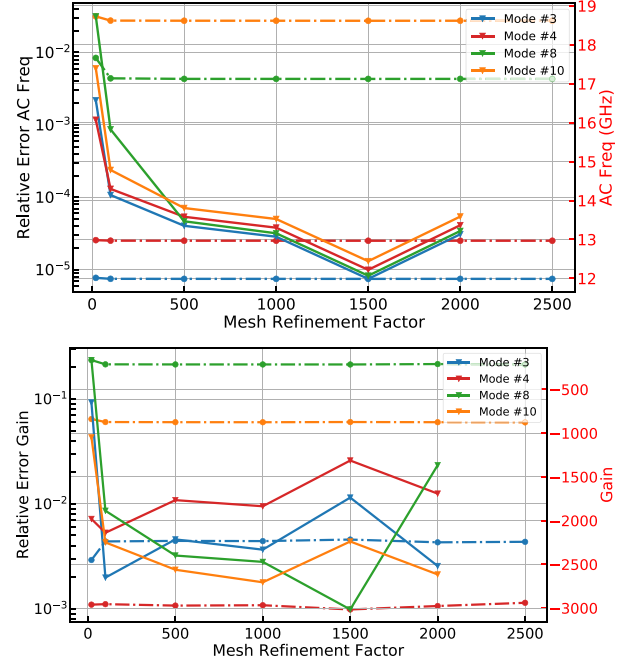

Fig. 18. Convergence of elastic mode frequency and SBS peak gain in rectangular silicon waveguide.

A. Equations of Elastic Waves

The complex displacement vector $\mathbf{u}(\mathbf{r}, t)$ of an elastic field undergoing harmonic oscillation takes the form:

$$\mathbf{u}(\mathbf{r}, t) = \mathbf{u}(x, y, z)\, e^{-i\,\Omega\, t} = \begin{bmatrix} u_x(x, y, z) \\ u_y(x, y, z) \\ u_z(x, y, z) \end{bmatrix} e^{-i\,\Omega\, t}, \quad (18)$$

where $\mathbf{r}$ is the position vector $\mathbf{r} = (x, y, z)$. The strain tensor $\mathbf{S}$ corresponding to the displacement vector $\mathbf{u}$ is

$$\mathbf{S} = \nabla_S\, \mathbf{u}, \quad (19)$$

$$= \frac{1}{2} \left(\nabla \mathbf{u} + (\nabla \mathbf{u})^T \right). \quad (20)$$

Hooke's Law states that the stress tensor $\mathbf{T}$ is linearly proportional to the strain tensor $\mathbf{S}$ (see Eq. (3.12), p. 43 in [18]):

$$\mathbf{T} = \mathbf{c} : \mathbf{S}, \quad (21)$$

where $\mathbf{c}$ is the fourth rank stiffness tensor characterizing the material.

In the frequency domain, i.e., $\mathbf{u}(\mathbf{r}, t) = \mathbf{u}(\mathbf{r})\, e^{-i\,\Omega\, t}$, the dynamical equation of elasticity in the absence of an external force is (See Eq. (2.18), p. 43 in [18])

$$\nabla \cdot \mathbf{T} + \Omega^2\, \rho\, \mathbf{u} = 0, \quad (22)$$

where ρ is the material density. In order to develop a finite element method solution, the wave equation Eq. (22) is written in weak form (variational formulation). We first take the product of Eq. (22) with the conjugate of a test function v, and integrate

over the domain A of the elastic field:

$$\int_A \boldsymbol{v}^* \cdot \left(\nabla \cdot \mathbf{T} + \Omega^2 \, \rho \, \mathbf{u} \right) \, dV = 0 \,. \tag{23}$$

Since the stress tensor $\mathbf{T}$ is symmetric, by applying the identity $\nabla \cdot (\mathbf{T} \, \boldsymbol{v}) = \boldsymbol{v} \cdot (\nabla \cdot \mathbf{T}) + \mathbf{T} : \nabla \boldsymbol{v}$, we are led to the following relation:

$$\boldsymbol{v}^* \cdot (\nabla \cdot \mathbf{T}) = \nabla \cdot (\mathbf{T} \, \boldsymbol{v}^*) - \nabla_S \boldsymbol{v}^* : \mathbf{T}, \tag{24}$$

where the operator : denotes the double dot product of two second-rank tensors [18]. In the derivation of Eq. (24), we have used the fact that the double dot product of the anti-symmetric part of $\nabla \boldsymbol{v}$ and tensor $\mathbf{T}$ is zero, since $\mathbf{T}$ is symmetric. By substituting Eq. (24) into Eq. (23) and applying the divergence theorem together with Eqs. (19) and (21), we obtain the following expression after integration by parts:

$$\int_A \left(-\nabla_S \boldsymbol{v}^* : (\mathbf{c} : \nabla_S \mathbf{u}) + \Omega^2 \, \rho \, \boldsymbol{v}^* \cdot \mathbf{u} \right) \, dA \\ + \int_{\partial A} \mathbf{n} \cdot (\mathbf{T} \, \boldsymbol{v}^*) \, dS = 0 \,, \tag{25}$$

where ∂A denotes the boundary of the domain A. The value of the boundary integral in Eq. (25) is zero when either of the following boundary conditions are applied to ∂A: the free interface condition $\mathbf{T} \cdot \mathbf{n} = \mathbf{0}$ or the fixed interface condition $\mathbf{u} = \mathbf{0}$.

B. Matrix Notation

Since the tensors $\mathbf{S}$ and $\mathbf{T}$ are symmetric, they possess only six independent coefficients and for numerical implementations, it is convenient to represent $\mathbf{S}$ and $\mathbf{T}$ as six-component vectors (Voigt notation):

$$\mathbf{S} = \begin{bmatrix} S_1 \\ S_2 \\ S_3 \\ S_4 \\ S_5 \\ S_6 \end{bmatrix} \quad \text{and} \quad \mathbf{T} = \begin{bmatrix} T_1 \\ T_2 \\ T_3 \\ T_4 \\ T_5 \\ T_6 \end{bmatrix}. \tag{26}$$

The coefficients $S_1, \ldots, S_6$ and $T_1, \ldots, T_6$ in Eq. (26) are defined by the relations [18]:

$$\mathbf{S} = \begin{bmatrix} S_{xx} & S_{xy} & S_{xz} \\ S_{xy} & S_{yy} & S_{yz} \\ S_{xz} & S_{yz} & S_{zz} \end{bmatrix} = \begin{bmatrix} S_1 & \frac{1}{2} S_6 & \frac{1}{2} S_5 \\ \frac{1}{2} S_6 & S_2 & \frac{1}{2} S_4 \\ \frac{1}{2} S_5 & \frac{1}{2} S_4 & S_3 \end{bmatrix}, \tag{27}$$

and

$$\mathbf{T} = \begin{bmatrix} T_{xx} & T_{xy} & T_{xz} \\ T_{xy} & T_{yy} & T_{yz} \\ T_{xz} & T_{yz} & T_{zz} \end{bmatrix} = \begin{bmatrix} T_1 & T_6 & T_5 \\ T_6 & T_2 & T_4 \\ T_5 & T_4 & T_3 \end{bmatrix}, \tag{28}$$

noting the absence of the $\frac{1}{2}$ factors in the stress tensor $\mathbf{T}$. In this matrix notation, the definition $\mathbf{S} = \nabla_S \mathbf{u}$ and the wave equation Eq. (25) still hold if the matrix form of the symmetric gradient

operator ∇_S is used:

$$\nabla_S \mathbf{u} = \begin{bmatrix} \dfrac{\partial}{\partial x} & 0 & 0 \\ 0 & \dfrac{\partial}{\partial y} & 0 \\ 0 & 0 & \dfrac{\partial}{\partial z} \\ 0 & \dfrac{\partial}{\partial z} & \dfrac{\partial}{\partial y} \\ \dfrac{\partial}{\partial z} & 0 & \dfrac{\partial}{\partial x} \\ \dfrac{\partial}{\partial y} & \dfrac{\partial}{\partial x} & 0 \end{bmatrix} \begin{bmatrix} u_x \\ u_y \\ u_z \end{bmatrix}. \tag{29}$$

In the matrix notation, the fourth rank stiffness tensor $\mathbf{c}$ becomes a matrix of order 6×6. For example, in media of monoclinic symmetry with one symmetry plane (xy), Hooke's Law can be written as

$$\begin{bmatrix} T_1 \\ T_2 \\ T_3 \\ T_4 \\ T_5 \\ T_6 \end{bmatrix} = \begin{bmatrix} c_{11} & c_{12} & c_{13} & 0 & 0 & c_{16} \\ c_{21} & c_{22} & c_{23} & 0 & 0 & c_{26} \\ c_{31} & c_{32} & c_{33} & 0 & 0 & c_{36} \\ 0 & 0 & 0 & c_{44} & c_{45} & 0 \\ 0 & 0 & 0 & c_{45} & c_{55} & 0 \\ c_{61} & c_{62} & c_{63} & 0 & 0 & c_{66} \end{bmatrix} \begin{bmatrix} S_1 \\ S_2 \\ S_3 \\ S_4 \\ S_5 \\ S_6 \end{bmatrix}, \tag{30}$$

where the coefficients c_{IJ} are the elastic stiffness constants of the material in the Voigt notation [18]. In this notation, the two subscripts I and J stand for the four subscripts of the fourth rank stiffness tensor c_{ijkl} in pairs ij and kl according to the mapping: $1 \rightarrow 11, 2 \rightarrow 22, 3 \rightarrow 33, 4 \rightarrow 23, 5 \rightarrow 13, 6 \rightarrow 12$. So for example, $c_{11} \rightarrow c_{1111}$, $c_{16} \rightarrow c_{1112}$, and $c_{45} \rightarrow c_{2313}$.

C. Waveguide Modes

For elastic waveguide modes, the displacement vector $\mathbf{u}(\mathbf{r}, t)$ takes the form

$$\mathbf{u}(\mathbf{r}, t) = \mathbf{u}(x, y) \, e^{i \, (q \, z - \Omega \, t)} \\ = \begin{bmatrix} u_x(x, y) \\ u_y(x, y) \\ u_z(x, y) \end{bmatrix} e^{i \, (q \, z - \Omega \, t)}, \tag{31}$$

where q is the propagation constant. Since the waveguide mode $\mathbf{u}$ has an exponential z-dependence, the symmetric gradient

operator in Eq. (29) now takes the form:

$$\nabla_S \mathbf{u} = \begin{bmatrix} \dfrac{\partial}{\partial x} & 0 & 0 \\[2mm] 0 & \dfrac{\partial}{\partial y} & 0 \\[2mm] 0 & 0 & i\,q \\[2mm] 0 & i\,q & \dfrac{\partial}{\partial y} \\[2mm] i\,q & 0 & \dfrac{\partial}{\partial x} \\[2mm] \dfrac{\partial}{\partial y} & \dfrac{\partial}{\partial x} & 0 \end{bmatrix} \begin{bmatrix} u_x \\[2mm] u_y \\[2mm] u_z \end{bmatrix}. \tag{32}$$

For the problems considered in this work, the propagation constant q has a fixed value and the associated frequency Ω is the unknown eigenvalue. By imposing the free interface condition $\mathbf{T} \cdot \mathbf{n} = \mathbf{0}$ (or the fixed interface condition $\mathbf{u} = \mathbf{0}$) at the waveguide wall and using the wave equation Eq. (25), we are led to the following eigenvalue problem:

For a given value of q, find $\Omega \in \mathbb{C}$ and $\mathbf{u} \in \mathcal{U}$ such that $\mathbf{u} \neq \mathbf{0}$ and $\forall \boldsymbol{v} \in \mathcal{U}$

$$\int_A (\nabla_S \boldsymbol{v})^* : (\boldsymbol{c} : \nabla_S \mathbf{u})\, \mathrm{d}A = \Omega^2 \int_A \rho\, \boldsymbol{v}^* \cdot \mathbf{u}\, \mathrm{d}A, \tag{33}$$

where $A \subset \mathbb{R}^2$ is the cross-section of the waveguide and $\mathcal{U}$ is the set of admissible solutions.

For $q \neq 0$, we adopt the following change of variable

$$u_z = i\,q\,\hat{u}_z, \tag{34}$$

which simplifies the algebraic manipulation. With the new variable $\hat{u}_z$, the symmetric gradient operator Eq. (32) can be expressed as

$$\nabla_S \mathbf{u} = \begin{bmatrix} \dfrac{\partial}{\partial x} & 0 & 0 \\[2mm] 0 & \dfrac{\partial}{\partial y} & 0 \\[2mm] 0 & 0 & -q^2 \\[2mm] 0 & i\,q & i\,q\dfrac{\partial}{\partial y} \\[2mm] i\,q & 0 & i\,q\dfrac{\partial}{\partial x} \\[2mm] \dfrac{\partial}{\partial y} & \dfrac{\partial}{\partial x} & 0 \end{bmatrix} \begin{bmatrix} u_x \\[2mm] u_y \\[2mm] \hat{u}_z \end{bmatrix}. \tag{35}$$

The variable $\hat{u}_z$ is particularly useful for eigenproblems where the frequency Ω in Eq. (33) is fixed to a given value while the propagation constant q is the unknown eigenvalue. Indeed, with the original displacement component u_z, this eigenproblem is nonlinear (as it involves both q and q^2). But, with the variable $\hat{u}_z$, the eigenproblem can be transformed into a linear eigenproblem where q^2 is the unknown eigenvalue, if the propagation medium has a monoclinic symmetry, i.e., when the matrix $\mathbf{c}$ has the profile

shown in Eq. (30). This result can be shown in a similar way to the derivation in [6] for electromagnetic waveguides.

D. Numerical Implementation

The numerical computation of acoustic modes in waveguides can be performed in several ways, for example using finite differences [30]. Here we adopt a finite element approach similar to the one described in [31]. The finite element method is based on the approximation of the functional space $\mathcal{U}$ by a finite-dimensional space $\mathcal{U}_h \subset \mathcal{U}$. When a set of basis functions $(\boldsymbol{g}_m)_{m=1,\ldots,\dim(\mathcal{U}_h)}$ is chosen, a field $\boldsymbol{g}_h$ inside the cross-section A can be represented as

$$\boldsymbol{g}_h = \sum_{m=1}^{\dim(\mathcal{U}_{\mathrm{h}})} u_m\, \boldsymbol{g}_m. \tag{36}$$

If we denote by $\mathbf{u}_h$ the vector of expansion components $(u_m)_{m=1,\ldots,\dim(\mathcal{U}_h)}$, the application of classical finite element procedures to the continuous problem Eq. (33) leads to the following finite dimensional eigenproblem:

$$\boldsymbol{K}\,\mathbf{u}_h = \Omega^2\, \boldsymbol{M}\,\mathbf{u}_h, \tag{37}$$

where, for $l, m \in \{1, \ldots, \dim(\mathcal{U}_h)\}$, the elements of the matrices $\boldsymbol{K}$ and $\boldsymbol{M}$ are defined as

$$K_{lm} = \int_A (\nabla_S \boldsymbol{g}_l)^* : (\mathbf{c} : \nabla_S \boldsymbol{g}_m)\, \mathrm{d}A, \tag{38}$$

$$M_{lm} = \int_A \rho\, \boldsymbol{g}_l^* \cdot \boldsymbol{g}_m\, \mathrm{d}A. \tag{39}$$

For the computer implementation, we have used basis functions $(\boldsymbol{g}_m)_{m=1,\ldots,\dim(\mathcal{U}_h)}$ which are piecewise quadratic polynomials. The generalized eigenvalue problem Eq. (37) can be solved using the eigensolver for sparse matrices ARPACK [22]. ARPACK requires a linear system solver and we have relied on the direct solver for sparse matrices UMFPACK [19]. The finite element meshes were generated with the software Gmsh [21].

REFERENCES

[1] B. Eggleton, C. Poulton, and R. Pant, "Inducing and harnessing stimulated Brillouin scattering in photonic integrated circuits," *Adv. Opt. Photon.*, vol. 5, pp. 536–587, 2013.
[2] P. T. Rakich, C. Reinke, R. Camacho, P. Davids, and Z. Wang, "Giant enhancement of stimulated Brillouin scattering in the subwavelength limit," *Phys. Rev. X*, vol. 2, 2012, Art. no. 011008.
[3] R. V. Laer, A. Bazin, B. Kuyken, R. Baets, and D. V. Thourhout, "Net on-chip Brillouin gain based on suspended silicon nanowires," *New J. Phys.*, vol. 17, 2015, Art. no. 115005.
[4] C. Wolff, M. J. Steel, and C. G. Poulton, "Formal selection rules for Brillouin scattering in integrated waveguides and structured fibers," *Opt. Express*, vol. 22, pp. 32489–32501, 2014.
[5] B. C. P. Sturmberg *et al.*, "Numbat—The numerical Brillouin analysis tool," 2018. [Online]. Available: https://github.com/bjornsturmberg/Numbat

[6] K. Dossou and M. Fontaine, "A high order isoparametric finite element method for the computation of waveguide modes," *Comput. Method. Appl. Mech. Eng.*, vol. 194, pp. 837–858, 2005.

[7] C. Wolff, R. V. Laer, M. J. Steel, B. J. Eggleton, and C. G. Poulton, "Brillouin resonance broadening due to structural variations in nanoscale waveguides," *New J. Phys.*, vol. 18, 2016, Art. no. 25006.

[8] P. Dainese *et al.*, "Stimulated Brillouin scattering from multi-GHz-guided acoustic phonons in nanostructured photonic crystal fibres," *Nat. Phys.*, vol. 2, pp. 388–392, 2006.

[9] P. T. Rakich, P. Davids, and Z. Wang, "Tailoring optical forces in waveguides through radiation pressure and electrostrictive forces," *Opt. Express*, vol. 18, pp. 14439–14453, 2010.

[10] C. Wolff, M. J. Steel, B. J. Eggleton, and C. G. Poulton, "Stimulated Brillouin scattering in integrated photonic waveguides: Forces, scattering mechanisms and coupled mode analysis," *Phys. Rev. A*, vol. 92, 2015, Art. no. 013836.

[11] V. Laude and J.-C. Beugnot, "Generation of phonons from electrostriction in small-core optical waveguides," *AIP Adv.*, vol. 3, 2013, Art. no. 042109.

[12] J.-C. Beugnot, S. Lebrun, G. Pauliat, H. Maillotte, V. Laude, and T. Sylvestre, "Brillouin light scattering from surface acoustic waves in a subwavelength-diameter optical fibre," *Nat. Commun.*, vol. 5, 2014, Art. no. 5242.

[13] Y. Pennec *et al.*, "Modeling light-sound interaction in nanoscale cavities and waveguides," *Nanophotonics*, vol. 3, pp. 413–440, 2014.

[14] J.-C. Beugnot and T. Sylvestre, "Shaping Brillouin light in specialty optical fibers," in *Shaping Light in Nonlinear Optical Fibers*, S. Boscolo and C. Finot, Eds. New York, NY, USA:Wiley, 2017.

[15] O. Florez *et al.*, "Brillouin scattering self-cancellation," *Nat. Commun.*, vol. 7, 2016, Art. no. 11759.

[16] J. E. Sipe and M. J. Steel, "A Hamiltonian treatment of stimulated Brillouin scattering in nanoscale integrated waveguides," *New J. Phys.*, vol. 18, 2016, Art. no. 045004.

[17] B. C. P. Sturmberg *et al.*, "Numbat—The Numerical Brillouin Analysis Tool, Documentation," 2018. [Online]. Available: https://numbat-au.readthedocs.io/en/latest

[18] B. A. Auld, *Acoustic Fields and Waves in Solids*, 2nd ed., vol. 1, Malabar, FL, USA: Krieger, 1990.

[19] T. A. Davis, "A column pre-ordering strategy for the unsymmetric-pattern multifrontal method," *ACM Trans. Math. Softw.*, vol. 30, pp. 165–195, 2004.

[20] P. Peterson, "F2PY: A tool for connecting Fortran and Python programs," *Int. J. Comp. Sci. Eng.*, vol. 4, pp. 296–305, 2009.

[21] C. Geuzaine and J. F. Remacle, "GMSH: A three-dimensional finite element mesh generator with built-in pre- and post-processing facilities," *Int. J. Numer. Meth. Eng.*, vol. 71, pp. 1309–1331, 2009.

[22] R. B. Lehoucq, D. C. Sorensen, and C. Yang, *ARPACK Users' Guide—Solution of Large-Scale Eigenvalue Problems With Implicitly Restarted Arnoldi Methods*. Philadelphia, PA, USA: SIAM, 1998.

[23] R. V. Laer, B. Kuyken, D. V. Thourhout, and R. Baets, "Interaction between light and highly confined hypersound in a silicon photonic nanowire," *Nat. Photon.*, vol. 9, pp. 199–203, 2015.

[24] E. A. Kittlaus, N. T. Otterstrom, and P. T. Rakich, "On-chip inter-modal Brillouin scattering," *Nat. Commun.*, vol. 8, 2017, art. no. 15 819.

[25] B. Morrison *et al.*, "Compact Brillouin devices through hybrid integration on silicon," *Optica*, vol. 4, pp. 847–854, 2017.

[26] M. J. A. Smith, B. T. Kuhlmey, C. M. de Sterke, C. Wolff, M. Lapine, and C. G. Poulton, "Metamaterial control of stimulated Brillouin scattering," *Opt. Lett.*, vol. 41, pp. 2338–2341, 2016.

[27] A. Choudhary *et al.*, "Advanced integrated microwave signal processing with giant on-chip Brillouin gain," *J. Lightw. Technol.*, vol. 35, no. 4, pp. 846–854, Feb. 2017.

[28] M. J. A. Smith, C. M. De Sterke, C. Wolff, M. Lapine, and C. G. Poulton, "Enhanced acousto-optic properties in layered media," *Phys. Rev. B*, vol. 96, 2017, Art. no. 064114.

[29] M. Malinowski and S. Fathpour, "Fully-tensorial modeling of stimulated Brillouin scattering in photonic waveguides," *IEEE J. Quantum Electron.*, vol. 55, no. 3, 2019, Art. no. 600107.

[30] N. Dostart, Y. Liu, and M. A. Popović, "Acoustic waveguide eigenmode solver based on a staggered-grid finite-difference method," *Sci. Rep.*, vol. 7, 2017, Art. no. 17509.

[31] A.-C. Hladky-Hennion, "Finite element analysis of the propagation of acoustic waves in waveguides," *J. Sound Vib.*, vol. 194, pp. 119–136, 1996.